ChemComm

COMMUNICATION

View Article Online
View Journal | View Issue

Cite this: *Chem. Commun.*, 2025, 61, 12199

Received 12th June 2025,
Accepted 9th July 2025

DOI: 10.1039/d5cc03323c

rsc.li/chemcomm

Divalent transition metal ion intercalated hydrated V_2O_5 nanosheet cathodes for ultra-long cycling aqueous zinc-ion batteries†

Jie Bai,[a] Wenting Ji,[b] Mengda Xue,[a] De Li,*[b] Huayu Wang[a] and Lingyun Chen*[a]

Given the rich d-electron structures of transition metals, we synthesized Co^{2+}/Ni^{2+}/Cu^{2+}-intercalated hydrated V_2O_5 nanosheet cathodes *via* a novel self-assembly approach, achieving excellent performance in AZIBs. DFT calculations revealed that the intercalation of transition metal ions modulates the electronic structure near the Fermi level of pristine V_2O_5, increasing DOS and reducing the band gap, thereby improving electrical conductivity.

The accelerated advancements in large-scale energy storage and flexible electronic devices have spurred a substantial demand for sophisticated rechargeable battery systems beyond lithium-ion technology.[1,2] Aqueous zinc-ion batteries (AZIBs) have garnered considerable attention among the next generation of energy storage units,[3–5] owing to the impressive theoretical specific capacities (820 mA h g^{-1} and 5854 mA h cm^{-3}) and low redox potential (−0.763 V *versus* the standard hydrogen electrode) of the metallic zinc anode, as well as the enhanced safety and cost-effectiveness of AZIBs.[6–9] Vanadium-based compounds have garnered significant attention due to their remarkable advantages in specific capacity, positioning them as promising candidates for cathode materials in next-generation large-scale AZIB energy storage systems.[4,10] Moreover, the work of Yuan *et al.* has substantially advanced and broadened the systematic investigation of cathode modification and anode protection in AZIBs.[11–13]

Layered materials have been extensively recognized in the field of electrochemical energy storage due to their abundant and tunable intercalation chemistry, as well as their high active surface.[14–17] In addition, their two-dimensional (2D) nanosheets, with thicknesses ranging from monolayer to multilayer, offer broad opportunities for subsequent structural and functional modifications.[18] Vanadium pentoxide (V_2O_5), as a representative layered vanadium oxide, possesses a high theoretical specific capacity of 589 mA h g^{-1} due to its variable valence states (from 5+ to 3+), which renders it widely utilized as a cathode material in AZIBs.[19] Research indicates that metal cations embedded into the layered structure of vanadium pentoxide serve as effective pillars within the structural framework, while also expanding the interlayer spacing and achieving exceptional zinc ion transport kinetics and storage capabilities.[20] Additionally, the incorporation of metal cations can effectively modulate the electronic structure near the Fermi level of pristine V_2O_5, enhancing its electrical conductivity, thereby improving electrochemical performance.[21,22] Notably, as intercalation ion candidates, transition metal cations have garnered significant attention due to their rich d-electron structures.[23,24] For instance, Bai *et al.* synthesized Cu^{2+} and Mn^{2+} co-intercalated hydrated V_2O_5 cathode materials, which exhibited superior Zn^{2+} diffusion kinetics and long cycling stability in AZIBs.[23] Herein, we demonstrate a hydrosol ion-mediated self-assembly strategy enabling the successful intercalation of three transition metal cations (Co^{2+}, Ni^{2+}, and Cu^{2+}) into the layered architecture of a hydrated V_2O_5 nanosheet, while preserving their structural integrity and ion-transport functionality. Moreover, compared to hydrothermal/solvothermal synthesis approaches, this self-assembly synthesis strategy enables the formation of a uniform phase structure.[20]

X-ray diffraction (XRD) patterns of the Co^{2+}, Ni^{2+}, and Cu^{2+} assembling products are given in Fig. 1a. The sharp peaks near 5–9° can be identified as the (001) characteristic peaks. XRD analyses reveal that, compared to pure V_2O_5 prepared by freeze-drying, the incorporation of Co^{2+} (13.2 Å), Ni^{2+} (13.4 Å), and Cu^{2+} (11.9 Å) ions induces a leftward shift of the (001) characteristic peak, indicating an expansion of the interlayer spacing. Fourier transform infrared (FTIR) and Raman spectra also confirmed the successful synthesis of the three products (Fig. S1 and S2, ESI†). X-ray photoelectron spectroscopy (XPS) analyses further confirmed the successful intercalation of Co^{2+},

[a] *Department of Applied Chemistry, School of Chemistry and Chemical Engineering, Chongqing University, Chongqing 401331, China. E-mail: lychen@cqu.edu.cn*
[b] *State Key Laboratory of Marine Resources Utilization in South China Sea, Key Laboratory of Research on Utilization of Si-Zr-Ti Resources of Hainan Province, School of Materials Science and Engineering, Hainan University, Haikou 570228, China. E-mail: lidehainu@hainanu.edu.cn*

† Electronic supplementary information (ESI) available. See DOI: https://doi.org/10.1039/d5cc03323c

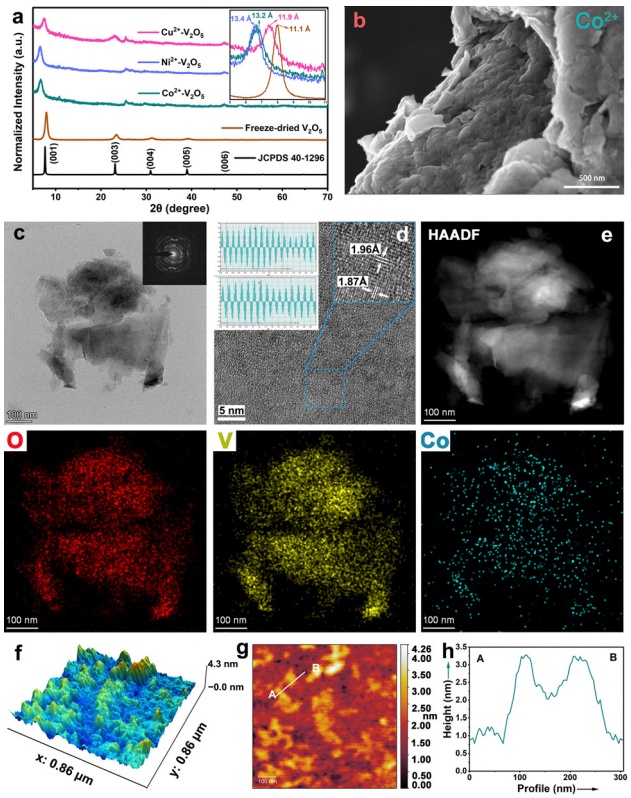

Fig. 1 (a) XRD patterns of the freeze dried V_2O_5 and Co^{2+}, Ni^{2+}, and Cu^{2+}, cooperative self-assembly products, respectively. (b) The FESEM image, (c) TEM image and corresponding selected area electron diffraction (SAED) pattern, (d) HRTEM image, (e) EDS mapping images, (f) and (g) AFM images and (h) corresponding height profiles of the Co^{2+} self-assembly sample.

Ni^{2+}, and Cu^{2+} (Fig. S3, ESI†). The field emission scanning electron microscopy (FESEM) and environmental scanning electron microscopy (ESEM) observations of the self-assembled samples reveal that their microscopic morphology exhibits large aggregates formed by the stacking of V_2O_5 nanosheets (Fig. 1b and Fig. S4, ESI†). The transmission electron microscopy (TEM) image of the Co^{2+} intercalated product (Fig. 1c) also reveals a two-dimensional nanosheet morphology. The high-resolution transmission electron microscopy (HRTEM) image captured from the surface of the nanosheets in Fig. 1d reveals well-defined 2D lattice fringes, with spacings of 0.187 and 0.196 nm corresponding to the interlayer spacings of the (006) planes of layered V_2O_5. The energy dispersive spectrum (EDS) mapping (Fig. 1e) demonstrates the uniform distribution of V, O, and Co elements within the sample, while the presence of Co distribution confirms the successful intercalation of Co^{2+} into the layered $V_2O_5{\cdot}nH_2O$ host. Atomic force microscopy (AFM) characterization revealed that the self-assembled Co^{2+} product exhibits a thickness ranging from 2.0 to 3.5 nm, confirming its two-dimensional stacked nanosheet structure, which is consistent with the findings from SEM analysis (Fig. 1f–h). The chemical formula of pristine $V_2O_5{\cdot}nH_2O$ and these samples intercalated by Co^{2+}, Ni^{2+}, and Cu^{2+} was determined by inductive coupled plasma (ICP) analysis (Table S1, ESI†) and thermogravimetric analysis (TGA) (Fig. S5, ESI†), which can be identified as $V_2O_5{\cdot}0.77H_2O$, $Co_{0.14}V_2O_5{\cdot}0.95H_2O$, $Ni_{0.15}V_2O_5{\cdot}0.63H_2O$, and $Cu_{0.15}V_2O_5{\cdot}0.60H_2O$, respectively.

Subsequently, the self-assembled samples were employed as cathode materials to assemble AZIBs using a 2 M $Zn(OTF)_2$ electrolyte and a zinc foil. According to a previous study,[20] the specific capacity of self-assembled products is highly dependent on the aging time following the self-assembly process. Therefore, we systematically investigated the impact of aging time after the Co^{2+} self-assembly process and conducted electrochemical evaluations. Galvanostatic charge–discharge (GCD) testing at 0.05 A g^{-1} revealed that the sample aged for 5 h exhibited the optimal capacity performance, further confirming the critical influence of aging time on the specific capacity (Fig. S6, ESI†). Consequently, an aging time of 5 h was ultimately adopted for all self-assembled products. Cyclic voltammetry (CV) tests demonstrated that $Co_{0.14}V_2O_5{\cdot}0.95H_2O$, $Ni_{0.15}V_2O_5{\cdot}0.63H_2O$ and $Cu_{0.15}V_2O_5{\cdot}0.60H_2O$ all exhibited pronounced redox peaks, indicative of typical battery behavior (Fig. 2a, and Fig. S7, ESI†). Compared to the pristine V_2O_5 prepared by direct freeze-drying, the rate performance tests of Co^{2+}, Ni^{2+}, and Cu^{2+} self-assembled samples exhibit superior discharge specific capacities (Fig. 2b). This enhancement is likely attributed to the modulation of the electronic structure of the pristine V_2O_5 by the rich d-electron of the transition metals, leading to improved conductivity. The $Co_{0.14}V_2O_5{\cdot}0.95H_2O$ cathode exhibited the highest discharge-specific capacity, which achieved average specific capacities of 338.2, 298.3, 260.8, 229.5, and 208.8 mA h g^{-1} at current densities of 0.1, 0.2, 0.4, 0.7, and 1.0 A g^{-1}, respectively. When the current density was reset to 0.1 A g^{-1}, the specific capacity recovered to 304.7 mA h g^{-1}. Notably, the $Co_{0.14}V_2O_5{\cdot}0.95H_2O$ cathode exhibited an outstanding discharge specific capacity of 373.2 mA h g^{-1} at a current density of 0.05 A g^{-1} (Fig. 2c). The electrochemical performance outlined above still presents certain advantages compared to previously

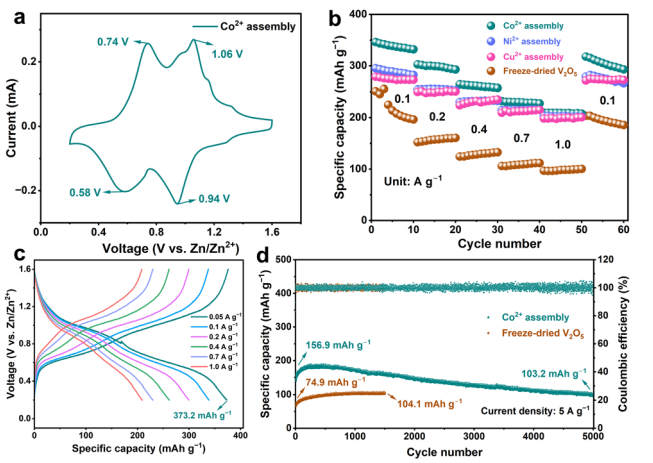

Fig. 2 (a) CV profile. (b) The corresponding rate performance profiles of Co^{2+}, Ni^{2+} and Cu^{2+} cathodes. (c) The corresponding GCD profiles at various current densities of the $Co_{0.14}V_2O_5{\cdot}0.95H_2O$ cathode. (d) Long-term cycling stability at 5.0 A g^{-1} of $Co_{0.14}V_2O_5{\cdot}0.95H_2O$ and freeze-dried V_2O_5 cathodes.

published studies (Table S2, ESI†). The assembled $Co_{0.14}V_2O_5{\cdot}0.95H_2O$, $Ni_{0.15}V_2O_5{\cdot}0.63H_2O$, and $Cu_{0.15}V_2O_5{\cdot}0.60H_2O$ cathodes were subjected to high-current long-term cycling performance tests (Fig. 2d, and Fig. S8, ESI†). It is noteworthy that the Co^{2+} self-assembled sample demonstrates superior cycling performance. The $Co_{0.14}V_2O_5{\cdot}0.95H_2O$ cathode retains a discharge-specific capacity of 103.2 mA h g^{-1} even after 5000 cycles at a current density of 5 A g^{-1}. The excellent cycling stability under high current density could be attributed to the appropriate interlayer spacing adjustment induced by Co^{2+} intercalation, as well as the pillaring effect between Co^{2+} and the host frame.[20] The GCD curves and low-current cycling performance profiles of the $Co_{0.14}V_2O_5{\cdot}0.95H_2O$ electrode further exemplify this characteristic (Fig. S9, ESI†).

A series of electrochemical evaluations confirmed that the $Co_{0.14}V_2O_5{\cdot}0.95H_2O$ cathode exhibits the optimal electrochemical performance among the self-assembled products derived from the three transition metal cations. Compared with Ni^{2+} and Cu^{2+}, Co^{2+} demonstrates superior electrochemical activity and stability due to its unique d-electron configuration, appropriate electrochemical potential, and robust Co–O bonds. These attributes contribute to more efficient charge transfer processes, thereby affording enhanced electrochemical performance. To further investigate the zinc ion storage and diffusion mechanisms of this self-assembly series, kinetic analyses were conducted. The CV curves of the $Zn/Co_{0.14}V_2O_5{\cdot}0.95H_2O$ battery were measured at different scan rates (Fig. 3a and Notes S1, ESI†). As shown in Fig. 3b, the *b* values of peaks 1 to 4 are 0.792, 0.791, 0.790, and 0.935, respectively, indicating that the storage of Zn^{2+} is predominantly governed by capacitive contributions. CV measurements at various scan rates indicate that the contribution of capacitive behavior becomes increasingly dominant with the increase in scan rate (Fig. 3c and d and Fig. S10, Notes S2, ESI†). The above results demonstrate that the Zn^{2+} storage kinetics in the $Zn/Co_{0.14}V_2O_5{\cdot}0.95H_2O$ battery are predominantly governed by capacitive behavior. In addition,

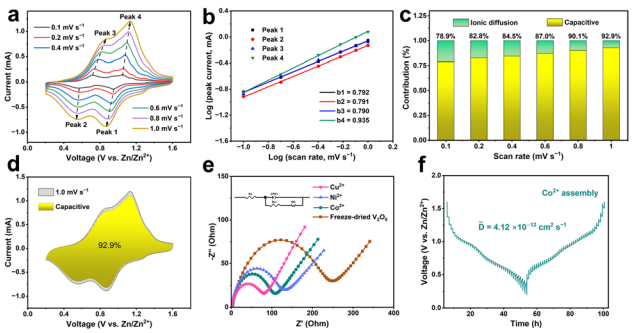

Fig. 3 (a) CV curves at various scan rates, (b) the as-calculated *b* value of four different peaks 1–4, (c) capacitive and diffusion contribution bar graph calculated from the dependence of peak current density and the scan rate, and (d) CV curves containing the schematic of capacitive contribution at a current density of 1.0 mV s^{-1}, for the $Co_{0.14}V_2O_5{\cdot}0.95H_2O$ cathode. (e) EIS spectrum of freeze-dried V_2O_5, $Co_{0.14}V_2O_5{\cdot}0.95H_2O$, $Ni_{0.15}V_2O_5{\cdot}0.63H_2O$ and $Cu_{0.15}V_2O_5{\cdot}0.60H_2O$ cathodes. (f) GITT analysis of the $Co_{0.14}V_2O_5{\cdot}0.95H_2O$ electrode.

electrochemical impedance spectroscopy (EIS) measurements were conducted to elucidate the charge transfer resistance (R_{ct}). The R_{ct} values of $Co_{0.14}V_2O_5{\cdot}0.95H_2O$, $Ni_{0.15}V_2O_5{\cdot}0.63H_2O$, and $Cu_{0.15}V_2O_5{\cdot}0.60H_2O$ are 92.7, 111.3 and 74.3 Ω, respectively, all of which are notably lower than that of the freeze-dried pristine sample ($V_2O_5{\cdot}0.77H_2O$, 225.1 Ω) (Fig. 3e). Notably, the average ion diffusion coefficient ($\bar{D}_{Zn^{2+}}$) value of $Co_{0.14}V_2O_5{\cdot}0.95H_2O$, as determined by the galvanostatic intermittent titration technique (GITT), is higher than those of $Ni_{0.15}V_2O_5{\cdot}0.63H_2O$, $Cu_{0.15}V_2O_5{\cdot}0.60H_2O$, and freeze-dried V_2O_5 (Fig. 3f and Fig. S11, Notes S3, ESI†). These results are consistent with the aforementioned unique electronic structure of Co^{2+}.

The density functional theory (DFT) calculation results indicated that the insertion of Co^{2+} modulates the electronic structure of pristine V_2O_5, reducing its band gap and enhancing its electrical conductivity (Fig. S12, ESI†). This leads to superior charge transfer kinetics in Co^{2+}-intercalated V_2O_5. The EIS measurements of $V_2O_5{\cdot}0.77H_2O$ and $Co_{0.14}V_2O_5{\cdot}0.95H_2O$ further corroborated these computational findings. *Ex situ* XRD characterization and XPS spectra further confirmed the typical Zn^{2+} intercalation/de-intercalation mechanism of the $Co_{0.14}V_2O_5{\cdot}0.95H_2O$ cathode, which is consistent with that of most previously reported vanadium-based cathodes (Fig. S13, ESI†). In summary, the electrochemical reaction mechanism of $Co_{0.14}V_2O_5{\cdot}0.95H_2O$ as a cathode for AZIBs can be delineated as shown in Fig. S14 (ESI†). The anodic reaction of the $Zn/Co_{0.14}V_2O_5{\cdot}0.95H_2O$ cell is a typical process of metallic zinc losing electrons ($Zn \rightarrow Zn^{2+} + xe^-$). We further performed ESEM analysis on different states of the first GCD cycle of the $Co_{0.14}V_2O_5{\cdot}0.95H_2O$ cathode at a current density of 0.1 A g^{-1} (Fig. S15, ESI†). The formation of products distinct from the original cathode material at different discharge states is also consistent with the aforementioned *ex situ* XRD and XPS characterization results. Furthermore, the investigations of *in situ* optical microscopy (OM) unambiguously corroborated the exceptional structural stability of the $Co_{0.14}V_2O_5{\cdot}0.95H_2O$ electrode, as evidenced by its preserved dimensional integrity throughout prolonged electrochemical cycling under intercalation/de-intercalation conditions (Fig. 4, and Notes S4, ESI†).

In conclusion, using a novel hydrosol ion-mediated self-assembly strategy, we successfully intercalated three transition metal cations (Co^{2+}, Ni^{2+}, and Cu^{2+}) into the layered framework of hydrated vanadium pentoxide ($V_2O_5{\cdot}nH_2O$) nanosheets. The self-assembled product of Co^{2+} demonstrates superior electrochemical performance, outperforming the self-assembled products of Ni^{2+} and Cu^{2+}, which can be attributed to its high electrochemical activity and excellent structural stability. DFT calculation results indicated that Co^{2+}-intercalated V_2O_5 exhibits an enhanced electronic DOS near the Fermi level and a reduced band gap value, enhancing the electrical conductivity of pristine V_2O_5. Electrochemical testing results demonstrated that the $Co_{0.14}V_2O_5{\cdot}0.95H_2O$ cathode retains a high discharge specific capacity of 103.2 mA h g^{-1} even after 5,000 cycles at a high current density of 5 A g^{-1}. Our work provides valuable insights into the development of high-performance vanadium-based cathode materials for aqueous batteries.

Jie Bai: writing – original draft, software, methodology, investigation, formal analysis, and data curation. Wenting Ji:

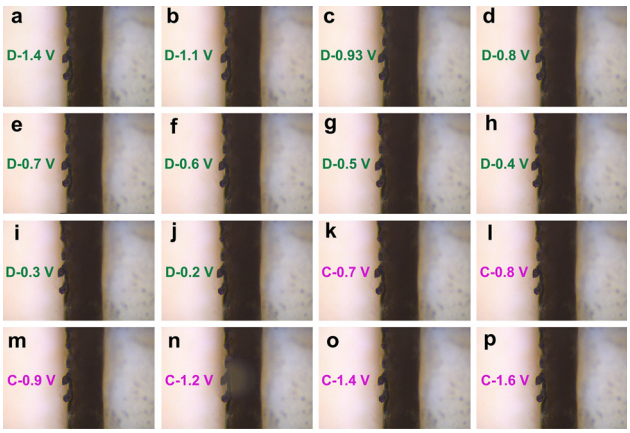

Fig. 4 The *in situ* OM characterization of the $Co_{0.14}V_2O_5{\cdot}0.95H_2O$ cathode. (a)–(j) correspond to discharge to 0.2 V, while (k)–(p) corresponds to charge to 1.6 V.

data curation, software, and formal analysis. Mengda Xue: data curation. De Li: data curation and software. Huayu Wang: data curation and analysis. Lingyun Chen: conceptualization, funding acquisition, supervision, validation, writing – review and editing.

The authors gratefully acknowledge financial support from the National Natural Science Foundation of China (No. 21676036), the Natural Science Foundation of Chongqing (No. CSTB2023NSCQ-MSX0580), and the Large-scale Equipment Sharing Fund of Chongqing University (No. 202403150240 and 202503150091). Thanks to Professor Xiaohua Chen (School of Chemistry and Chemical Engineering, Chongqing University) for his help in DFT calculations. And we would like to thank Dr. Wei Yin at Analytical and Testing Center of Chongqing University for her assistance with ICP analysis.

Conflicts of interest

There are no conflicts to declare.

Data availability

The data that support the findings of this study are available in the ESI.†

Notes and references

1 Y. Liang, H. Dong, D. Aurbach and Y. Yao, *Nat. Energy*, 2020, **5**, 646–656.
2 R. Service, *Science*, 2021, **372**, 890–891.
3 Z. Zhao, R. Wang, C. Peng, W. Chen, T. Wu, B. Hu, W. Weng, Y. Yao, J. Zeng, Z. Chen, P. Liu, Y. Liu, G. Li, J. Guo, H. Lu and Z. Guo, *Nat. Commun.*, 2021, **12**, 6606.
4 Y. Kim, Y. Park, M. Kim, J. Lee, K. Kim and J. Choi, *Nat. Commun.*, 2022, **13**, 2371.
5 S. Jin, Y. Shao, X. Gao, P. Chen, J. Zheng, S. Hong, J. Yin, Y. Joo and L. Archer, *Sci. Adv.*, 2022, **8**, 4456.
6 L. Ma, M. Schroeder, O. Borodin, T. Pollard, M. Ding, C. Wang and K. Xu, *Nat. Energy*, 2020, **5**, 743–749.
7 L. Wang, K. Huang, J. Chen and J. Zheng, *Sci. Adv.*, 2019, **5**, 4279.
8 H. Dong, J. Li, J. Guo, F. Lai, F. Zhao, Y. Jiao, D. Brett, T. Liu, G. He and I. Parkin, *Adv. Mater.*, 2021, **33**, 2007548.
9 C. Liu, J. Zeng, S. Di, S. Wang and L. Li, *Acta Mater.*, 2024, **281**, 120433.
10 R. Service, *Science*, 2018, **362**, 508–509.
11 H. Chen, Y. Wang, S. Zhang, Y. He, L. Hou and C. Yuan, *Chem. Eng. J.*, 2024, **479**, 147422.
12 S. Zhang, X. Jia, F. Chu, L. Hou and C. Yuan, *Small*, 2025, **21**, 2500321.
13 X. Gao, Y. Liu, M. Shen, X. Liu, Y. Zhao, L. Hou and C. Yuan, *Adv. Funct. Mater.*, 2025, 2503212.
14 L. Wang, K. Takada, A. Kajiyama, M. Onoda, Y. Michiue, L. Zhang, M. Watanabe and T. Sasaki, *Chem. Mater.*, 2003, **15**, 4508–4514.
15 R. Ma, X. Liu, J. Liang, Y. Bando and T. Sasaki, *Adv. Mater.*, 2014, **26**, 4173–4178.
16 R. Li, F. Xing, T. Li, H. Zhang, J. Yan, Q. Zheng and X. Li, *Energy Storage Mater.*, 2021, **38**, 590–598.
17 Y. Dang, F. Zhu, D. Wang, S. Yu, Y. Wei and D. Han, *Acta Mater.*, 2025, **284**, 120588.
18 P. Xiong, B. Sun, N. Sakai, R. Ma, T. Sasaki, S. Wang, J. Zhang and G. Wang, *Adv. Mater.*, 2020, **32**, 1902654.
19 C. Liu, Z. Neale, J. Zheng, X. Jia, J. Huang, M. Yan, M. Tian, M. Wang, J. Yang and G. Cao, *Energ. Environ. Sci.*, 2019, **12**, 2273–2285.
20 Y. Liu, C. Lu, Y. Yang, W. Chen, F. Ye, H. Dong, Y. Wu, R. Ma and L. Hu, *Adv. Mater.*, 2024, **36**, 2312982.
21 C. Xia, J. Guo, P. Li, X. Zhang and H. Alshareef, *Angew. Chem., Int. Ed.*, 2018, **57**, 3943–3948.
22 D. Dai, Y. Chen, B. Li, Z. Zhang, J. Wang, L. Wang, Y. Huang, B. Wang and D. Liu, *Small*, 2025, **21**, 2408596.
23 A. Wang, D. Liu, L. Yang, F. Xu, D. Luo, H. Dou, M. Song, C. Xu, B. Zhang, J. Zheng, Z. Chen and Z. Bai, *Carbon Energy*, 2024, **6**, e512.
24 H. Bandi, A. Kakarla, R. Dahule, R. Maezono, D. Narsimulu, R. Shanthappa and J. Yu, *Small*, 2025, **21**, 2408568.

